Tuning Oxygen Occupancy within Metal-Oxo Clusters for Enhancing Catalytic Activity of Zr-MOFs

Charlotte Simms,§ ‡† Angelo Mullaliu,§ ‡ Euan T. Sarson,§ †† ‡ Albert Solé-Daura,| Jordi Puiggalí-Jou,| Jorge J. Carbó,| Giuliana Aquilanti,|| and Tatjana N. Parac-Vogt§*

§Department of Chemistry, KU Leuven, Celestijnenlaan 200F, 3001 Leuven, Belgium

|Department de Quımica Fısica i Inorganica, Universitat Rovira i Virgili, Tarragona 43007, Spain

||Elettra –Sincrotrone Trieste, s.s. 14 - km 163,5 in AREA Science Park, 34149 Basovizza, Trieste, Italy

KEYWORDS: MOF, metal-oxo clusters, catalytic activity, EXAFS, DFT

ABSTRACT: Metal Organic Frameworks containing Lewis acidic metals such as Zr(IV) are highly promising biomimetic catalysis, able to perform a variety of biologically inspired reactions in a range of different environments. By modulating the building blocks of a parent MOF, structural changes can be induced that may result in increased catalytic activity. Typically, the organic components of the MOF are targeted for such modulation, either through removal of organic linkers or addition of functional groups. Modifying the inorganic component and transforming the nature of the inorganic cluster of the MOF in a controlled manner is more challenging and have been less explored as means of enhancing catalytic activity of MOFs. Here we demonstrate that tuning oxygen coordination within the metal-oxo cluster via post-synthetic exchange of Mg(II) into Zr_6O_8-MOF-808 in aqueous solution results in coordinatively unsaturated Zr(IV) metal sites with enhanced catalytic activity. Advanced structural characterization that include quantitative EXAFS analysis and detailed XRD Rietveld refinement, combined with computational studies based on DFT and DFT-based Molecular Dynamics, confirmed that single and double substitution of Zr(IV) with Mg(II) occurred within the cluster core. This resulted in formation of Zr_5MgO_8 and $Zr_4Mg_2O_7$ mixed metal-oxo catalytic sites with decreased overall oxygen occupancy due to the lower coordination number of Mg(II) compared to Zr (IV). The effect of substitution on cluster symmetry and stability has been investigated, and the mechanism of post-synthetic exchange, the stability of resulting structures, and enhancements to catalysis are supported by an in-depth computational study. We show both experimentally and using computational techniques that such modifications promote MOF-substrate interaction and decrease the activation energy (E_{act}) for catalyzing biologically relevant reactions such as hydrolysis of peptide bonds and dephosphorylation of amino acids. This work presents a innovative strategy for enhancement of MOF catalytic activity through controlled modulation of the inorganic cluster and demonstrates that the reduced oxygen occupancy of a cluster promotes more efficient catalysis.

Introduction

A substantial amount of modern industrial processes rely on some form of catalysis in order to reduce energy consumption and improve the sustainability and efficiency of processes, both to minimize energy costs, and to reduce the ecological effects of the processes.[1-3] Nature also relies heavily on highly efficient catalysis through production of specific enzymes to carry out cellular functions essential to life.[4, 5] Inspired by nature, the field of catalysis often relies on applying naturally occurring enzymes to develop and enhance their industrial processes. Many natural enzymes have been already used, such for example renin for milk fermentation, phospholipase for biodiesel production, and penicillin amidase for drug production.[6, 7] Although enzyme engineering has made great strides in utilizing these natural enzymes through up-scaled production and increased durability, they still suffer from considerable shortcomings such as reduced long-term stability, fixed (and often limiting) substrate specificity, poor re-usability, and need for multi-step recovery procedures from reaction mixture.[8] Thus, development of artificial enzymes is of key interest to a wide range of industries. Ideally, these artificial enzymes should have efficiency and selectivity of natural enzymes, whilst overcoming their aforementioned limitations. Arising from this need, the field of nanozymes[9-17] emerged with the aim of developing low-cost, reusable, and tunable enzyme

mimics. The class of materials that shows exceptional promise is Metal Organic Frameworks (MOFs), which are highly crystalline, porous, organic-inorganic hybrid materials, formed of metal ions or inorganic clusters bridged by organic linkers, that result into large 2D or 3D structures. These inorganic clusters are typically formed from highly Lewis acidic metal ions such as Zr(IV), Ce(IV), or Hf(IV) and bridging μ_3-O species, forming M_6O_8 clusters. Organic linkers featuring carboxylic or amide end-groups form strong interactions with the clusters, resulting in robust structures. One of the key characteristics of MOFs is their exceptionally high surface area, and unlike other catalytic materials such as nanoparticles, where catalysis is limited to the solvent exposed external surface areas, the porosity of MOFs can increases the accessible surface area up to 7,000 m^2/g.[18]

MOFs have demonstrated excellent ability to serve as catalysts for a variety of organic reactions, including oxidation, acetalization, cyanosilylation, and epoxide alcoholysis. [19, 20] In addition, they can mimic the reactivity of naturally occurring enzymes such as hydrolases,[21] oxidases[22] and peroxidases.[23] As hydrolytic nanozymes, MOFs have excelled at both hydrolysis of peptide bonds and hydrolysis of phosphate bonds in a variety of natural and synthetic substrates under many different conditions.[24-27] Many studies have demonstrated that the hydrolytic activity of MOFs can be enhanced through structural modifications of the parent MOF via creation of missing linker defects[28-30], control over the surface area and particle size[31], or through the introduction of more active functional groups present on the organic linkers.[26, 32]

In contrast, studies that focus on the controlled modifications of the metal cluster to enhance catalysis are much more scarce. Several studies have shown that incorporation of a second metal into the MOF cluster can either enhance the reactivity of parent MOF, or give the MOF an additional reactivity feature.[22, 33-36] Examples of successful incorporation of a second metal to enhance activity of a MOF include synthesis of the bimetallic Ni/Co clusters in MOFs for use as positive electrode materials[37], Zr/Ti-UiO-66 for alcohol oxidation[38-40], Cu/Rh-BTC for propylene hydrogenation[41], MOF-74(Cu/Co) for styrene oxidation[42], Eu/Yb/Gd-TCPB for NO sensing[43], Mo/Zr-UiO-66 for dye removal from waste water[44], Fe/Zr-UiO-66 for water decontamination[45] and MIL-100(Fe, Ni) as Prins reaction catalysis.[46] We have extensively explored the use of Zr-MOFs as nanozymes for the hydrolysis of peptide bonds in peptides and proteins, and have shown that structural fine-tuning can be used to enhance activity and control over the MOF-substrate interaction.[22, 30-32, 47-50] For example, by using of the bimetallic Zr/Ce- UiO-66[22] and Zr/Ce-MOF-808[51] we demonstrated that the presence Ce(IV), which has greater coordination flexibility in comparison to Zr(IV), resulted in more efficient nanozymatic activity.

Inspired by these findings, here we envisioned a novel strategy to enhance the activity of the MOF through generation of open metal sites, by forming coordinatively unsaturated clusters via incorporation of a metal ion with a lower coordination number. This approach had already been demonstrated by Gil-San-Millan *et al.*[52] where Mg(II) was exchanged with Zr(IV) in MOF-808 and NU-1000.

Such an approach is distinct from previous works that demonstrated that the generation of missing linker defects leads to enhanced catalysis through generation of open metal sites on the metal clusters, often at the expense of material stability. In this work we show that the activity of Zr-MOFs could be enhanced by inserting a different metal ion that does not necessarily play active part in catalysis, without relying on the generation of missing linkers. We hypothesized that the presence of an ion such as Mg(II), in place of one or two Zr(IV) centers in the cluster would lower the number of oxygen bridges between incorporated Mg(II) and the neighboring Zr(IV) ions, due to the lower coordination number of Mg(II) (CN=6) compared to Zr(IV) (CN=8). Such substitution would make substrate binding with the catalytically active Zr(IV) centers more accessible, as the Zr(IV) would be coordinatively unsaturated, and as such, enhance catalysis without reducing the number of organic bridges that maintain the MOF's structure.

Insertion of Mg(II) into the Zr_6O_8 cluster into parent MOF-808 has been demonstrated before, using a synthesis with DMF and formic acid at high temperature and pressure resulting in enhanced hydrolysis of phosphate bonds.[53] In the previous work, the formation of a single substituted $MgZr_5O_8$ cluster was identified via EXAFS analysis, and increasing the concentration of $Mg(OMe)_2$ in the exchange solution led to generation of additional single substituted clusters of the same type. In this study, the parent MOF-808 was synthesized under much milder conditions using water as a solvent at lower temperature,[54] and the PSE method to incorporate Mg(II) was selected over direct hydrothermal synthesis in order to minimize the structural changes in the resulting M_6O_8 cluster that may be caused by different coordination geometries of Zr(IV) and Mg(II) and the presence of the much smaller Mg(II) ion. In addition, we pushed the boundaries of PSE by incorporating a second Mg(II) in the MOF-808 SBU by inducing double substitution of Zr(IV) for Mg(II), which resulted in formation of a discrete $Zr_4Mg_2O_7$ cluster, in contrast to the previous studies. We thoroughly investigated the structural effect that Mg(II) incorporation has on the cluster's structure, and demonstrate that inserting the less Lewis acidic ion, Mg(II) into Zr-MOF induces structural changes on a discrete cluster level that ultimately promote catalytic activity.

A challenging task was to unambiguously confirm that Mg(II) was indeed incorporated into the cluster in place of Zr(IV), rather than being grafted onto the Zr_6O_8 cluster. This was achieved through an advanced characterization methodology comprising of detailed XRD Rietveld refinement and analysis of the parent and PSE-modified MOFs using EXAFS and a DFT study of the exchange. Following the thorough characterization of the MOF materials, their activity was tested towards the hydrolysis of peptide and phosphoester bonds in different biomolecules. The structural and reactivity findings were combined with a detailed computational study to fully understand the effect of single and

double substituted Mg(II) as a co-factor in these materials, revealing that the lower coordination number of Mg(II) causes a reduced oxygen occupancy of the mixed metal clusters within the MOF, rationalizing how the presence of a less Lewis acidic metal ion in the cluster can increase catalytic activity of the material. Significantly, and in contrast to previous work with bimetallic Zr/Ce-MOF-808 which used structurally similar Ce(IV) and Zr(IV) metals, resulting in MOFs that almost exclusively contained either mono-metallic Zr_6O_8/Ce_6O_8 clusters or a mono-substituted Zr_5CeO_8 cluster, the PSE method developed here allowed for double substitution and formation of the $Zr_4Mg_2O_7$ cluster to occur. Such double substitution, along with similar structural features compared to the parent Zr-MOF-808 and reduced oxygen occupancy on the cluster, opens up a new avenue for catalytic enhancement of MOFs without relying on modulation of the organic components of the MOF or undermining structural stability by increasing the number of defects.

Methods

Experimental procedures

All chemicals were commercially obtained and used without further purification. Reactions were performed without any precautions against air and moisture. Computational methods are detailed in the supporting information.

Zr-MOF-808 Synthesis

MOF-808 was synthesised using the method of Reinsch and co-workers.[55] A mixture of trimesic acid (1.33 mmol, 280 mg), $ZrOCl_2{\cdot}8H_2O$ (4 mmol, 1.288 g), water (10 mL), and acetic acid (10 mL) was heated at 95 °C in sealed Synthware 48 mL high pressure vessels for 18 h while stirring. The white precipitate was collected via centrifugation (5000 rpm, 25 min), redispersed in $NaOAc_{(aq)}$ (15 mL, 0.1 M; twice), and water (15 mL; once). After which, it was redispersed in acetone (5 mL; once) and dried overnight at 70 °C.

Post-synthetic Exchange of Metals

Post synthetic exchange of Mg for Zr within the MOF was attained by following the method of Gil-San-Millan and co-workers.[52] A mixture of MOF-808 (300 mg), $Mg(OMe)_2$/MeOH (468 μL, 7-10 wt%), and MeOH (15 mL) was shaken for 15 min to afford **Mg1-Zr**. **Mg2-Zr** was made using the same method but with double the volume of $Mg(OMe)_2$/MeOH (936 μL, 7-10 wt%). The white precipitates of **Mg1-Zr** and **Mg2-Zr** were collected via centrifugation (5000 rpm, 25 min), and washed with MeOH (15 mL, x 3).

Activation of MOFs

MOFs were dried for 3 h at 70 °C and then activated over 17 h at 120 °C prior to analysis and catalysis.

Characterisation

Inductively Coupled Plasma Optical Emission Spectroscopy (ICP-OES) - **Mg1-Zr** (50 mg) and **Mg2-Zr** (50 mg) were each digested using a mixture of HCl (5 mL, 47%), HNO_3 (4 mL, 70%), and HBF_4 (2 mL, 28%) in a Mars 6 microwave digester with a ramp time of 10 min and a hold time of 25 min at 210 °C (pre-set zeolite program). An aliquot of 0.5 mL was diluted to 10 mL with ultra-pure water prior to measurement. Measurements were recorded in a 2% HNO_3 matrix. MOF pKa Measurements - MOF (10 mg) was equilibrated in $NaNO_{3(aq)}$ (12 mL of 0.01 M solution) for 20 min with stirring.[56] The mixture was adjusted to pH 3 using $HCl_{(aq)}$ (0.1 M solution) and then titrated with $NaOH_{(aq)}$ (0.1 M solution) to pH 11 at a rate of 10 μL/min with gentle stirring. pH was recorded just before the following NaOH addition.

XRD Analysis

X-ray diffraction (XRD) patterns were recorded on a PanAnalytical diffractometer equipped with a Cu Kα source (γ = 0.15406 nm) in the $1.3° < 2\theta < 45.0°$ range with a step size of 0.013°. Rietveld refinement was conducted using GSAS-II software.[57]The structural model reported by Furukawa et al.[58] was used in the refinement after excluding the solvent molecules: μ3-O are either oxo (O_2 and O_3) or hydroxyl ligands (O_7 and O0AA), while μ2-O derived from the modulator and linker are labeled as O_4 and O_1, respectively. The instrumental parameters were obtained from a LaB_6 standard; accordingly, the Gaussian instrument broadening parameters, i.e., U, V, and W, were fixed to $1.109{\cdot}10^{-4}$ deg^2, $-2.22{\cdot}10^{-4}$ deg^2, $4.956{\cdot}10^{-4}$ deg^2, respectively. The Cauchy instrument broadening parameters, i.e., X and Y, were fixed to 0 deg. The Finger-Cox-Jephcoat low-angle peak asymmetry parameter, SH/L, was kept fixed to the optimised value of 0.038. The peak shape was refined with a generalised microstrain broadening model and by optimising the respective parameters. Atomic displacement values for Zr and Mg were constrained to be equal, and the same was done for the remaining O and C atoms. Occupancies of Zr and Mg were fixed to the experimental values retrieved via ICP analysis. The scale, background, sample displacement, unit cell parameters, peak shape, and atomic parameters were refined in this order.

XAFS Analysis

XAFS experiments were performed at the XAFS 11.1 beamline of Elettra - Sincrotrone Trieste (Italy).[59] The storage ring operated at 2.4 GeV in top-up mode with a typical current of 310 mA. XAFS data were recorded at the Zr K-edge in transmission mode using pellets made upon mixing a proper amount of Zr/Mg MOFs and cellulose. Spectra were acquired from 17698 eV to 19522 eV around the Zr K-edge with a constant k-step of 0.03 $Å^{-1}$ and 2s/point acquisition time.

The extended X-ray absorption fine structure (EXAFS) analysis was performed using the GNXAS package based on the multiple scattering (MS) theory.[60, 61] The sinusoidal signal of the experimental EXAFS spectra was described by considering only a few key contributions. Two two-body ($\gamma^{(2)}$) term signals were used to account for the two different structural oxygens in the Zr first-shell environment ($\gamma_1^{(2)}$) (Zr-O1) and ($\gamma_2^{(2)}$) (Zr-O2)), while an additional two-body signal was used to describe the Zr-Zr contribution in the second-shell sphere ($\gamma_3^{(2)}$) (Zr-Zr)). In the EXAFS fitting, the degeneracy of γ_1 and γ_3 scattering contributions were refined while maintaining fixed γ_2 to consider the difference in signal after the post-synthetic exchange of Zr with Mg. Notably, the scattering power of Mg (Z = 12) is significantly lower than the respective for Zr (Z = 40), which is used here to detect Mg insertion in the cluster while looking at the decrease of Zr-M (M = Zr/Mg) scattering term.

Activity Studies

Hydrolysis reactions were performed in 4.0 mL screw cap vials with PTFE stirring bars. Glycylglycine Hydrolysis - MOF (6 μmol) was added to a solution of glycylglycine (3.00 mL of 2 mM D_2O stock solution) and stirred for 20 min to finely disperse the MOF particles in solution. The pD was adjusted to 7.4 with NaOD and DCl. The reaction mixture was heated at 60 °C with stirring for 5 h and aliquots of 550 μL were taken at 0.5 h, 1 h, 2 h, 3 h, and 5 h. The reaction kinetics were followed by ^{1}H-NMR. pX Hydrolysis - MOF (6 μmol) was added to a solution of pX (pX = pSer or pTyr; 3.00 mL of 8 mM D_2O stock solution) and stirred for 20 min to finely disperse the MOF particles in solution. The pD was adjusted to 7.4 with NaOD and DCl. The reaction mixture was heated at 60 °C with stirring for 240 h and aliquots of 550 μL were taken at 17 h, 72 h, 96 h, 144 h, and 240 h.

The reaction kinetics were followed by ^{1}H-NMR. MOF Peptidase vs Phosphatase Activity Study - Solutions of Gly-Gly and pSer, and Gly-Gly and pTyr, (3.00 mL of 8 mM D_2O stock solution) were prepared, to which MOF (6 μmol) was added and stirred for 20 min to finely disperse the MOF particles in solution. The pD was adjusted to 7.4 with NaOD and DCl. The reaction mixture was heated at 60 °C with stirring for 5 h and aliquots of 550 μL were taken at 0.5 h, 1 h, 2 h, 3 h, and 5 h. The reaction kinetics were followed by ^{1}H NMR.

Results and Discussion

Synthesis and Characterization of Zr_5MgO_8 and $Zr_4Mg_2O_7$ based MOF-808

Preparation of the mixed metal MOFs was carried out in two stages. Initially, the parent Zr-MOF-808 was synthesized using a one-pot green synthesis adapted from work by Reinsch and coworkers[54], followed by post-synthetic exchange (PSE) of Zr(IV) with Mg(II) present in solution from $Mg(OMe)_2$[53]. This two-step approach was chosen to ensure that the parent MOF-808 structure would be preserved, allowing the precise effect of Mg(II) on the structure and catalysis to be determined. As the coordination geometry and coordination number (CN) of Mg(II) (typically CN = 6) and zirconium(IV) (CN = 8) are different, we anticipated that using Mg(II) and Zr(IV) in a one-pot MOF synthesis, might not result in formation of M_6O_8 clusters, and instead would result in alternative MOF structures being produced. Indeed, to the best of our knowledge, Mg_6O_8 type clusters have not been reported so far. Resulting MOF materials were fully characterized before and after PSE to determine structural changes, and most importantly, to confirm that successful metal exchange of Zr(IV) with Mg(II), and not merely grafting of Mg(II) onto the parent MOF, occurred. The parent Zr-MOF-808 was synthesized in a mixture of water and acetic acid (1:1 ratio), in a sealed system at 95 °C for 18h, after which the MOF was collected, washed, and dried. Successful synthesis was confirmed through comparison of the PXRD pattern of the resulting MOF with the calculated pattern of MOF-808. Following the synthesis of the parent MOF, PSE of FZr(IV) for Mg(II) was achieved by soaking the parent MOF in varying amounts of $Mg(OMe)_2$ (2:1 and 4:1 Zr_6:Mg) dissolved in methanol. This resulted in two MOF-808s containing different amounts of Mg(II) within the clusters, referred to as **Mg1-Zr** and **Mg2-Zr**, while the parent MOF is referred to as **Zr**. As seen in the PXRD and SEM images (Figure 1), the PSE process did not affect the morphology of the MOF, nor the global crystalline structure. Particle size was also unaffected (Table 1), with the particles in all three MOFs averaging between 0.95 and 1.08 μm in diameter, as determined by scanning electron microscopy (SEM) micrographs. Using Inductively Coupled Plasma Optimal Emission Spectroscopy (ICP-OES) after acid digestion of the MOFs, the percentage of metal determined to be Mg in the PSE samples was found to be 15% and 33% (Table 1) for **Mg1-Zr** and **Mg2-Zr** respectively. This translates to cluster compositions of Zr_5Mg and Zr_4Mg_2 respectively, in agreement with the initial report by Gil-San-Millan.[53] The PSE process lead to a 25% reduction in BET surface area (Figure S1, Table 1), decreasing from 1983 m^2g^{-1} to 1498 m^2g^{-1} as the amount of Mg(II) increased. It should be noted that the surface area of both Mg-substituted MOFs was very similar, showing that the PSE process was responsible for the decrease in surface area rather than proportion of Mg(II) present. This is also reflected in similar particle sizes of **Mg1-Zr** and **Mg2-Zr**.

The surface area of **Mg2-Zr** in this work was larger than the surface areas previously reported for Mg/Zr-MOF-808 (1498 m^2g^{-1} vs 1290 m^2g^{-1}), although the reduction in surface area due to the PSE process was 25%, i.e. the same reduction as previously reported.[53] Additionally, no changes were seen in the pore size distribution (Figure S2), showing that the PSE process did not damage the porous interior of the MOF, in contrast to previous reports using the formic acid/DMF variant where significant changes to the pore distribution was described.[52] Thermogravimetric analysis (TGA) (Figure S4) confirmed that the thermal stability was also not affected by the PSE with Mg(II), highlighting a significant benefit of PSE to generate mixed metal MOFs. Using our PSE approach, the organic components of the MOF are less affected compared to other synthetic modification attempts, preserving the thermal resilience of the MOFs.[22, 51] As the presence of missing clusters was not detected in FT-IR (Figure S5), the number of missing linkers was calculated from the TGA traces, based on the weight loss above 300°C. The parent Zr-MOF-808 averaged 0.9 missing linkers per cluster, based on a maximum occupancy of 6, which increased to 1.26 for the two Mg-containing MOFs. This suggests that the PSE process reduced the coordination of the metals in the clusters within the MOFs equally, suggesting that observed structural changes are independent of Mg(II) concentration in the MOF's structure. Additionally, the change in acidity of the MOFs was determined using an acid-base titration, and three pKa values were determined based on the protocol by Farha et al.[62]

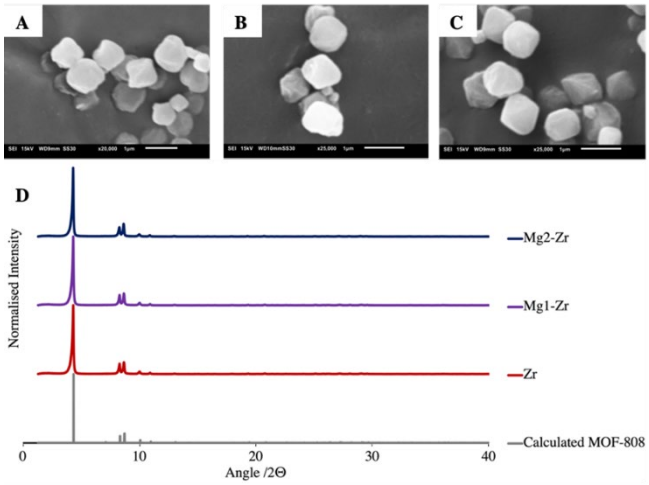

Figure 1: Initial structural characterization of Zr-MOF-808, and MOFs after PSE with Mg(II), forming **Mg1-Zr** and **Mg2-Zr**. SEM microscopy of A) **Zr**, B) **Mg1-Zr**, and C) **Mg2-Zr**. D) Experimental PXRD of the MOFs compared with the respective Rietveld refined patterns. The low residual is in line with the fit goodness retrieved through Rietveld refinement (cf. Table 2).

In Tables 1 and S5, it can be seen that the acidity decreases as more Mg(II) is incorporated (and less Zr(IV) is present) in the MOF, as the pKa of μ_3-OH and -OH increases by 0.23 and 0.21 respectively when comparing **Zr** and **Mg2-Zr**. This is in line with the exchange of Zr(IV) for the less Lewis acidic and more oxophilic Mg(II). To investigate our hypothesis that insertion of Mg(II) occurred at the cluster level by replacing Zr(IV), the ICP-OES analysis (Tables 1, S1) of the MOFs and exchange solutions after PSE was performed. The amount of Zr in the MOF sample decreased in correlation with the increase in Mg, suggesting that Mg was not doped onto the MOF surface, but rather substituted the Zr in some fashion. The release of Zr into solution during PSE was also recorded using ICP-OES and the data are presented in Table S1. The solution used for PSE showed an increase in Zr and decrease in Mg after the PSE process, again suggesting effective substitution of metals rather than grafting of Mg onto the MOF structure.

Table 1: Structural characterization of MOF-808 materials.

MOF	Zr_6:Mg[a]	Particle Diameter[b] (µm)	S_{BET}[c] (m^2g^{-1})	Missing linker per cluster[d]	pKa[e] μ_3-OH
Zr	1:0	1.07 ± 0.09	1783	0.90	3.32
Mg1-Zr	4:1	0.94 ± 0.07	1503	1.26	3.45
Mg2-Zr	2:1	0.94 ± 0.06	1498	1.26	3.55

From [a]ICP-OES, [b]SEM, [c]N_2 physisorption isotherms, [d]TGA (from a maximum of 6 linkers per cluster) [e]Acid-base titration.

In-depth structural analysis of the Zr/Mg mixed-metal MOFs was carried out by fitting the XRD patterns and the EXAFS spectra at the Zr K-edge, probing the long- and short-range structural order, respectively. The analysis corroborates the post-synthetic exchange of **Zr** with one (**Mg1-Zr**) or two Mg atoms (**Mg2-Zr**) per cluster and the increased free coordination sites around the Zr atoms induced by Mg doping. As shown in Table 2, the crystal lattice experiences a slight expansion due to Mg(II) insertion. While the lattice dimension, *a*, increases by roughly 0.3%, the lattice volume expands by approximately 1% after inserting one or two Mg ions per Zr_6O_8 cluster. Although Mg(II) is smaller than Zr(IV), the volume change might be due to structural strains in the long-range order, as probed by XRD. On the contrary, the local structure around Mg/Zr is affected differently, as confirmed by XRD Rietveld refinement and EXAFS fitting. Indeed, the Rietveld refinement results reported in Table 2, evidence a contraction of the Zr/Mg-O interatomic distance upon Mg(II) insertion, and are in good agreement with the EXAFS retrieved distances (cf. Table 3). Here, it is important to note that average Zr-O (~2.16 Å,[63]) and Mg-O (~2.11 Å,[64]) bond lengths in the respective oxides are comparable. Finally, XRD Rietveld refinement also provides an estimation of the amount of Zr/Mg, and refined atomic occupancies in Table 2 are in good agreement with the ICP-OES results reported in Table 1 and S1, further sustaining the hypothesis of successful PSE.

Table 2: Relevant XRD Rietveld refinement results. Residual (wR), lattice parameter (a), cell volume (V), calculated density (ρ_{calc}), atomic occupancies (Occ) for Zr and Mg, and Zr/Mg-O, and interatomic distances are reported for Zr, Mg1-Zr, and Mg2-Zr. Values in brackets indicate the error on the retrieved structural parameter.

		Zr	Mg1-Zr	Mg2-Zr
wR		0.1414	0.1251	0.1124
a / Å		35.17(19)	35.28(13)	35.27(12)
V / Å^3		43497(7)	43925(5)	43863(12)
ρ_{calc} / g.cm^{-3}		0.7425	0.6964	0.6560
Occ(Zr)		1.0 (fixed)	0.82(2)	0.68(2)
Occ(Mg)		0.0 (fixed)	0.18(9)	0.32(2)
Inter-atomic Distances	**Zr-μ_3O**	2.23(3)	2.21(3)	2.20(3)
	Zr-μ_2O	2.25(2)	2.22(2)	2.22(2)
	Mg-μ_3O	/	2.20(4)	2.20(3)
	Mg-μ_2O	/	2.21(2)	2.22(2)

With this information, complementary structural characterization was carried out using in-depth EXAFS analysis of the Zr K-edge to confirm Mg(II) incorporation into the cluster, and determine how the presence of Mg(II) affected the local environment of the catalytic site. The extracted EXAFS signal for **Zr**, **Mg1-Zr**, and **Mg2-Zr** was fitted by considering three main two-body ($\gamma^{(2)}$) contributions, as described in the Experimental section. The overall fit is presented in

Figure 2A-C, highlights a very good match between experimental and calculated signals. In general, a $\gamma_1^{(2)}$ signal with a four-fold degeneracy (N) is needed to characterize the Zr-μ_3-O1 fragment, a $\gamma_2^{(2)}$ signal describes the interaction between Zr and μ_2-O2 atoms (from the linker, substrate/product, solvent, or modulator, N = 4), and a $\gamma_3^{(2)}$ Zr-Zr (adjacent Zr atoms at around 3.5 Å, N = 4) is finally required for a Zr_6O_8 SBU model. From a qualitative point of view, the region between 8-14 $Å^{-1}$ is strongly affected by the Zr-Zr scattering term (γ_3), which in Figure 2A-C experiences a clear reduction in amplitude when increasing the Mg(II) content. This experimental evidence preannounces a clear-cut difference in the Zr-Zr degeneracy among the samples, and in particular, a lower Zr-Zr coordination number correlates to the increase of Mg(II) in the cluster. The Fourier transform (FT) of the EXAFS signal and the respective fit are reported in Figure 2D-F, visually emphasizing the difference among the samples. Indeed, the second peak in the FT, correlated to the second-shell coordination (Zr-Zr), is drastically affected by Mg(II) insertion, as shown by the downward arrow in panel F.

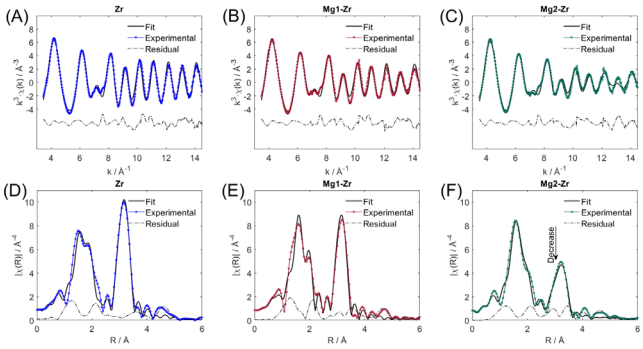

Figure 2: Extracted EXAFS signals for (A) **Zr**, (B) **Mg1-Zr**, and (C) **Mg2-Zr** and corresponding Fourier transforms (D-F).

Quantitative results of the EXAFS fitting are reported in Table 3. Several key parameters retrieved by the analysis highlight the structural modifications around the Zr(IV) local environment upon Mg(II) doping: (i) the drastic decrease in the degeneracy (N) of the γ_3 signal, due to the Zr-Zr scattering pair (from 4 in Zr to 3.2 in **Mg1-Zr**, and 2.4 **Mg2-Zr**); (ii) the significant contraction of the second-shell interatomic distance in **Mg2-Zr** (Zr-Zr = 3.55 Å); (iii) the drop in the degeneracy of γ_1, emphasizing that the lower coordination of Mg(II) induces an increase in free catalytic sites at the Zr(IV) ion; (iv) a reduction of the skewness parameter (β) for the Zr-Zr distribution in **Mg2-Zr**, indicating an increase of symmetry in the second-shell distribution.

Table 3: Relevant EXAFS fitting results for Zr, Mg1-Zr, and Mg2-Zr samples: interatomic distances (R), Debye-Waller factors (σ^2), degeneracy values (N), and skewness parameter (β). Values in brackets indicate the error on the retrieved structural parameter and were obtained by plotting contour plots within the selected 95% confidence interval.

		Zr	Mg1-Zr	Mg2-Zr
$\gamma_1^{(2)}$ (Zr-O1)	R / Å	2.174(13)	2.133(12)	2.158(15)
	σ^2 / Å^2	0.015(3)	0.008(3)	0.017(5)
	N	4.0(6)	3.3(4)	2.8(5)
$\gamma_2^{(2)}$(Zr-O2)	R / Å	2.248(12)	2.244(12)	2.225(11)
	σ^2 / Å^2	0.007(2)	0.006(2)	0.007(2)
	N	4 (fixed)	4 (fixed)	4 (fixed)
$\gamma_3^{(2)}$(Zr-Zr)	R / Å	3.61(2)	3.61(2)	3.55(3)
	σ^2 / Å^2	0.011(3)	0.012(3)	0.008(4)
	N	4(1)	3.2(9)	2.4(10)
	β§	1.2	1.3	0 (Gaussian)

§ The beta parameter (β) is the dimensionless skewness parameter directly related to the third cumulant of a skewed distribution. For β = 0, a Gaussian distribution is considered.

Considering the model of a Zr_6O_8 cluster, but with a single Mg(II) substituted, each Zr(IV) should theoretically be surrounded on average by 3.2 Zr atoms, as experimentally retrieved for **Mg1-Zr**. Theoretically, when a second substitution occurs, the degeneracy of the Zr-Zr, should drop to 2.5 in case of adjacent Mg atoms, or to 2 for a conformation with opposite Mg atoms. In **Mg2-Zr**, the obtained value for N(Zr-Zr) is 2.4, sustaining the assumption of a Zr_4Mg_2 metallic core, in agreement with the ICP results (Table 1). Furthermore, the decrease in N(Zr-O) indicates an average of 7.3 or 6.8 oxygen atoms in the SBU model for **Mg1-Zr** and **Mg2-Zr**, respectively. Hence, the introduction of Mg(II) into the cluster structure in place of Zr(IV) induces the decrease of overall oxygen occupancy due to the lower coordination of Mg(II) since the general coordination number of Mg is 6, compared with 7 or 8 for Zr.

Finally, the Debye-Waller (DW) factor (σ^2) and skewness parameter (β) for the γ_3 term of the **Mg2-Zr** cluster was determined. On one hand, the DW factor accounts for structural and thermal disorder and the lower value may indicate a diminution of the overall disorder for the Zr-Zr fragment; on the other hand, skewness on the Zr-Zr term is a measure of asymmetry of the second-shell atomic distribution, and a value of β = 0 suggests that the Zr-Zr distribution can be considered as Gaussian. Analysis of the **Mg2-Zr** cluster indicates a lower structural disorder and a more symmetric distribution for the Zr-Zr pairs in comparison to **Mg1-Zr** cluster, suggesting that **Mg1-Zr** is more unsymmetrical than **Mg2-Zr**.

From this, it was proposed that when the parent Zr-MOF-808 (Zr) undergoes PSE with a single Mg(II), the Mg(II) atom randomly replaces any of the six Zr atoms constituting the cluster (as shown in Figure 3). When exchanging a second Zr for an additional Mg (giving rise to **Mg2-Zr**), there are two possible structural conformations, with additional Mg being placed either adjacent to the first Mg or opposite to it. However, the low degree of structural asymmetry and disorder determined in the **Mg2-Zr** sample may preliminarily suggest that the cluster conformation where the Mg atoms are opposite to each other (bottom cluster in Figure 3)

is the most likely conformation to form. From this structural analysis of the cluster, the reduced oxygen occupancy around the Zr(IV) should leave them coordinately unsaturated and is expected to enhance the activity of the cluster, and therefore the entire MOF, towards catalysis. The charge imbalance of the metal ion due to unsaturation promotes hydration of the metal ion and substrate interaction, benefiting hydrolysis reactions in particular.

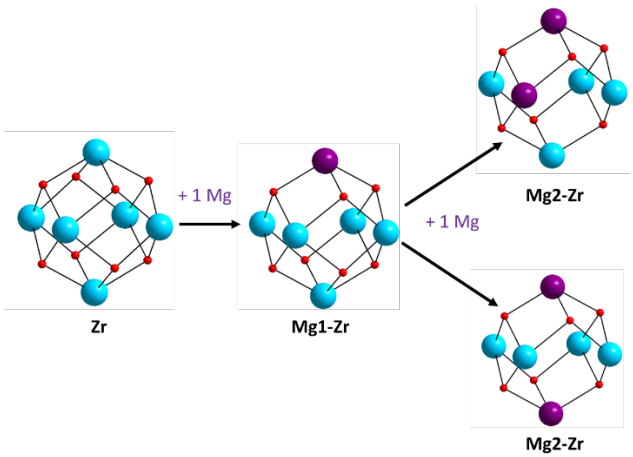

Figure 3: PSE of Mg into Zr-MOF-808. When a single Mg is exchanged (Mg1-Zr), substitution of any Zr is possible. When a second Mg is substituted (Mg2-Zr), it may be located Mg-adjacent (top), or Mg-opposite (bottom)

Computational study of the Mg(II)-by-Zr(IV) exchange in MOF-808

To further support our experimental findings, theoretical calculations were carried out to investigate the replacement of Zr(IV) by Mg(II) in the nodes of MOF-808 and its impact on the structure of the material. Firstly, Density Functional Theory (DFT) calculations were conducted to provide atomically-resolved structural information about the Mg(II)-containing metal-oxo nodes of the **Mg1-Zr** MOF. Based on the experimental characterization of the **Mg1-Zr** material, a model of its metal-oxo cluster was created from the crystal structure of the parent MOF-808[58] by replacing a ZrO^{2+} unit with a Mg(II) ion, saturating undercoordinated metal sites with

bridging acetate ligands. Geometry optimization within a 'cluster model' approach (see computational details) and accounting for solvent effects of methanol through a continuous dielectric medium, led to the structure represented in Figure 4a. Note that such a computational approach has been successfully adopted to investigate the reactivity of metal-oxo nodes in MOF chemistry.[65, 66] The Mg(II) ion was found to be accommodated in the distorted octahedral environment created by two carboxylate oxygens of two distinct linkers, one from an acetate ligand, and two hydroxo and one oxo groups from the metal oxo cluster. Notably, as illustrated in Figure 4b, one of the μ_3-OH groups, originally coordinated to three Zr(IV) ions in the Zr_6 [1] cluster, becomes a di-bridged ligand that connects Mg with a neighboring Zr center, and shifts towards the center between these two atoms to grant an octahedral environment for Mg. Such a rearrangement causes a slight decrease in the coordination numbers of Zr by O atoms in the nodes of **Mg1-Zr** as compared to the parent MOF, from 8 to 7.4 in average (see Figure S6), as obtained from the analysis of their optimized structures. However, as shown in Figure 4c, the metal replacement does not trigger significant distortions of the nodes and their overall structure and shape are preserved, further supporting the experimentally observed lack of crystallinity loss upon Mg incorporation.

DFT calculations were also performed to estimate the free-energy cost of the metal exchange process according to the following reaction (Eq. 1) occurring in methanol:

$$Zr_6 + [\mathbf{Mg}(OMe)_2(MeOH)_2] + MeOH \longrightarrow Zr_5Mg + [\mathbf{Zr}(\mathbf{O}H)(OMe)_3(MeOH)_2] \quad (1)$$

The structure and ligand environments of Mg(II) and Zr(IV) ions in methanol solution were determined by carrying out DFT-based Molecular Dynamics (DFT-MD) simulations of $[Mg(OMe)_2]$ and $[Zr(OH)(OMe)_3]$ salts embedded in explicit methanol solvent (see computational details section for further details). This situation represents Mg(II) complexes in the reactants state and released Zr(IV) complexes in the products, which are expected to reside in the solvent bulk rather than within the pores of the MOF. As shown in Figure S7, these simulations revealed a pseudo-tetrahedral coordination environment for Mg(II), in line with previous MD studies of Mg(II) ions in ethanol; [67] and a distorted octahedral environment for Zr(IV). Mg(II) was found to coordinate two anionic methoxy ligands and two methanol molecules; whereas Zr(IV) stabilizes two methanol molecules in a cis configuration, beside two methoxy ligands (exchanged with Mg), another one arising from the spontaneous deprotonation of a methanol molecule by the Zr=O group released from the MOF and, hence a hydroxo ligand. For Zr(IV) ions, Messner et al.[68] reported solvation spheres consisting of 8 water molecules based on MD simulations. However, the coordination numbers observed here, approximately 6 in methanol, can be rationalized by the bulkier nature of methoxy groups compared to water molecules. This hinderance limits the association of more than 6 ligands. As a matter of fact, MD simulations of Mg(II) in water predicted coordination numbers close to 6,[69] being consistently higher than that of 4 observed in methanol.[67] Note that coordination numbers to the metal ions in solution are lower than within the nodes of the MOF due to the distinct electronic and steric properties of their binding ligands. In fact, previous DFT-MD analyses showed that the coordination number of a Zr(IV) ion embedded in a polyoxometalate structure varies as a function of the electron-donating character of its ligands.

Using configurations obtained from DFT-MD trajectories for the metal complexes in solution, an affordable free-energy cost of +10.8 kcal.mol^{-1} could be estimated for the formal ZrO^{2+}-by- Mg^{2+} replacement. It is worth noting that the dimerization of Zr(IV) complexes in methanol (Figure S8),

was found to be strongly exergonic, by 25.2 kcal.mol^{-1}, compensating the still accessible cost of two sequential metal-exchange events (+21.6 kcal.mol^{-1}). Therefore, the latter might be expected to provide the thermodynamic driving force for the whole metal-exchange process. Thus, although characterizing the entire mechanism of such a complex process is beyond the scope of the present work, our calculations further support the feasibility of incorporating Mg(II) into the nodes of Zr_6O_8 based MOF-808, as inferred from experimental characterization.

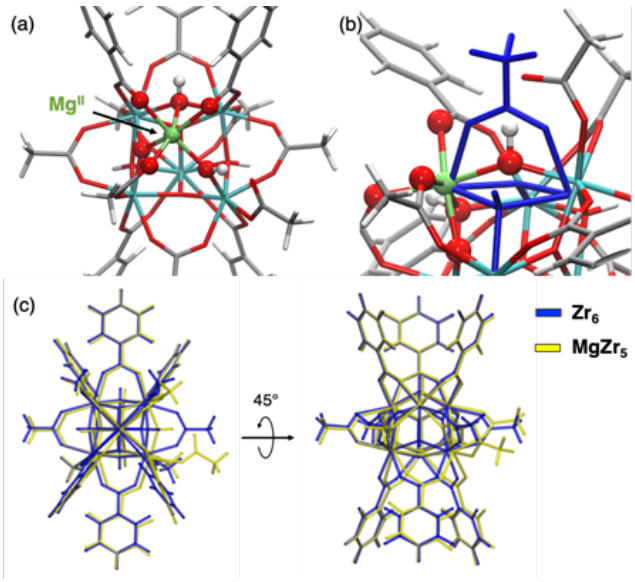

Figure 4: (a) Optimized structure of a $MgZr_5$ node of the **Mg1-Zr** MOF. The Mg(II) ion and the groups directly bonded to it are represented as spheres, while the rest of the structure is shown as sticks. Color code: Mg (lime), Zr (cyan), O (red), C (gray), H (white). (b) Closer look to the coordination environment of the embedded Mg(II) ion, where the configuration of the parent Zr_6 cluster is overlayed in blue sticks for comparison. (c) Two views of the superimposed models of Zr (blue) and Mg1-Zr (yellow) systems.

Reactivity towards Peptide Bond Hydrolysis

To confirm the predicted benefits that reduced oxygen occupancy in the Mg-containing clusters can have on the overall catalytic activity of the MOF, hydrolysis of glycylglycine (Gly-Gly) dipeptide was used as a model reaction, which allows for easy comparison with the previously reported MOF nanozymes.[70] Our group has already demonstrated that introducing the more Lewis acidic Ce(IV) into Zr-MOFs enhances their catalytic properties due to the increased coordination number of the Ce(IV) in the cluster, resulting in faster hydrolysis of Gly-Gly. Using the same model reaction, the effect of Mg(II) insertion into Zr-MOF-808 was tested by incubating 6 μmol MOF with an equimolar amount of Gly-Gly solution in D_2O at 50 - 80 ˚C, and following the hydrolysis of peptide bond with ^{1}H-NMR.

Indeed, the presence of increasing amounts of Mg(II) benefited the reactivity of the MOF towards Gly-Gly hydrolysis. Reactivity at different temperatures is presented in Figure 5A, and ^{1}H-NMR of Gly-Gly hydrolysis by **Zr** is presented in Figure S10. As temperatures increased, the enhancement of reactivity due to Mg(II) became more significant, particularly in the presence of **Mg2-Zr**. At 80 ˚C, the observed rate constant was calculated to be 1.59 x10^{-4} s^{-1}, giving a half-life of 1.21 hours, which represents an acceleration of more than four orders of magnitude compared to the uncatalyzed reaction.[71] As the number of missing linkers between **Mg1-Zr** and **Mg2-Zr** remained constant, and the particle size were similar, this increase in catalytic activity cannot be explained by changes to the organic component or the structural parameters of the MOF's structure. Several previous works have shown that changes to the organic components of MOFs result in structural modifications and influences catalytic activity of the MOFs.[70, 72-77] Thus, it is clear that the presence of Mg(II) is exerting influence over activity of the MOFs, as predicted based on the structural findings of reduced oxygen occupancy.

In comparison to previous work, the MOFs synthesized in this work (**Zr**, **Mg1-Zr**, and **Mg2-Zr**) outperform Zr-UiO-66 and Zr-NU-1000 by one and two orders of magnitude respectively, even when the reaction was carried out at the lower temperature of 50 ˚C, compared to 60 °C for UiO-66 and NU-1000.[50, 74] Additionally, MOFs in this work also outperformed the Zr/Ce-UiO-66[78], where the more Lewis acidic Ce(IV) made up 61% of total metal in the MOF.

A particularly interesting comparison to make is with the nano-sized MOF-808, having a particle size of just 35 nm and surface area of 1920 m^2/g, which was designed to maximize hydrolytic efficiency.[72] This nano-MOF gave a Gly-Gly hydrolysis rate comparable to the significantly larger **Mg2-Zr** with smaller BET surface area, demonstrating that incorporating Mg(II) into the MOF can influence the MOF's reactivity more than organic structural changes such as amount of defects, surface area, or particle size - all of which are determined through modulation of organic linker, solvent volume, and modulating acid used in the synthesis. Furthermore, the activation energy (E_a) of Gly-Gly hydrolysis was calculated using the Arrhenius equation, demonstrating that the presence of Mg(II) decreases the E_{act} from 18.0 kcal.mol^{-1} with the pure Zr MOF, to 12.0 kCal.mol^{-1} with the **Mg2-Zr** MOF, making the MOFs more effective catalysts (Figure 5B). This is a significant step forwards in the development of green MOFs for catalysis, as the **Mg2-Zr** MOF is synthesized without DMF and at lower temperatures, yet exhibits similar reactivity to the benchmark Zr-MOF-808[50] which was synthesized at high temperature, high pressure, in DMF and formic acid.

PXRD was recorded after hydrolysis to check the stability of the MOFs in the reaction conditions (Figure S11), and ICP-OES was used to determine the amount of metal ions leached from the MOFs during the reactions (Table S6). No significant changes were observed in the PXRD diffractograms and only a small amount of metal ion leaching was recorded (0.05 ppm Zr and 0.11 ppm Mg for Mg2-Zr) after 48 h reaction. As a control, the Mg(II) precursor,

$Mg(OMe)_2MeOH$, was also tested for catalytic activity towards GG hydrolysis and showed no reactivity after 7 days.

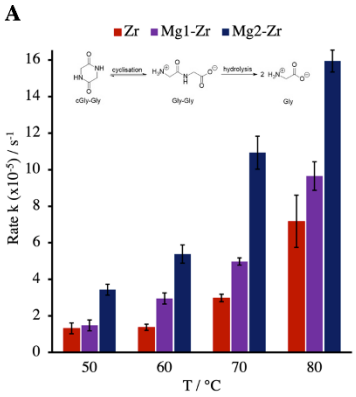

Figure 5: Peptide bond hydrolysis by MOFs **Zr**, **Mg1-Zr** and **Mg2-Zr**. A) hydrolysis rate at different temperatures, with reaction scheme. B) Calculated activation energy of reaction (E_a) Conditions: 6 μmol MOF, 3 mL 2mM Gly-Gly solution in D_2O, pD 7.4, with stirring.

Reactivity towards Phosphoester Hydrolysis

Since the introduction of Mg(II) into Zr-MOF-808 has been shown to have beneficial effect on their catalysis of nerve agents, which effectively resulted from their ability to hydrolyze P-F and P-S bonds,[52] the hydrolytic ability of MOF synthesized in this work was further tested for the hydrolysis of phosphoester bonds, which are frequently present in proteins as a result of post translational modifications (PTMs). Such modifications are important in cellular signaling acting as a molecular switch for the activation or inactivation of various cellular processes. The ability of MOF nanozymes to hydrolyze phosphoester bonds was tested using phosphorylated serine (pSerine) and tyrosine (pTyrosine) model substrates, since these amino acids are very prone to PTMs in proteins. Hydrolysis of phosphoester bond, which results in dephosphorylation of the substrate (Figure 6), was followed by ^{1}H-NMR spectroscopy (Figures S12 and S13), and the reaction parameters are represented in Table 4.

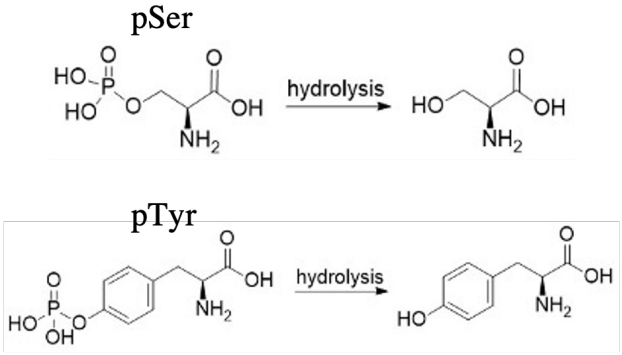

Figure 6: Hydrolysis of pSer and pTyr

As can be seen from the kinetic experiments, the presence of Mg in **Mg2-Zr** significantly increased the hydrolysis rate of pSer compared to both Zr-MOF catalyzed and the uncatalyzed reactions. In presence of **Mg2-Zr** the first order rate constant increased by two orders of magnitude compared to the uncatalyzed reaction, and one order of magnitude compared to the parent MOF **Zr**.

Table 4: Hydrolysis of pSer and pTyr by Zr and Mg2-Zr. Conditions: 6 μmol MOF, 3 mL 8 mM pX solution in D_2O, pD 7.4, 60 ˚C, with stirring.

Reaction Rate /s^{-1}	pSer Hydrolysis	pTyr Hydrolysis
Control	3.31×10^{-8}	1.71×10^{-8}
Zr	1.31×10^{-7}	3.43×10^{-7}
Mg2-Zr	2.36×10^{-6}	3.03×10^{-7}

Interestingly, the presence of Mg(II) had less pronounced influence on the hydrolysis of pTyr compared to the parent Zr-MOF. This is likely due to the presence of the aromatic side chain of Tyr which could result in significant adsorption of the amino acid onto the MOF through π-π stacking with the aromatic linker. This was evidenced using quantitative NMR analysis, where adsorption of pTyr onto **Zr** and **Mg2-Zr** was very similar (46% and 40% respectively). In contrast, the adsorption of pSer differed significantly between the two MOFs (57% for **Zr** and 27% for **Mg2-Zr**) suggesting that the reduced Lewis acidity of the Mg containing MOFs results in reduced adsorption of the non-aromatic substrate onto the MOF, thus promoting catalytic turnover. Stability of MOFs were determined after reaction using PXRD (Figures S14 and S15), where it was apparent that the increased adsorption of pTyr through interactions with the linker caused a drop in crystallinity to the MOFs as evidenced through PXRD.

The competition between hydrolysis of the peptide bond and phosphoester bond was also examined, since these bonds are often simultaneously present in proteins. **Zr** and **Mg2-Zr** MOFs were incubated both with Gly-Gly and pSer or pTyr at the same time, and after 1 h of reaction hydrolysis of the peptide bond in Gly-Gly was 100% complete, while no dephosphorylation occurred within this time frame. However, in the presence of GG and pTyr, **Zr** was only 63% selective towards Gly-Gly hydrolysis, while 37% of product was dephosphorylation Tyr. This was improved to a selectivity of 79% in the presence of **Mg2-Zr**, showing a significant reduction in dephosphorylation and promotion of peptide bond hydrolysis. This is most likely due to the increased adsorption of the aromatic pTyr onto the MOF, which results in enhanced MOF-substrate interaction. As such, the presence of Mg(II) within the MOFs can make the catalysts more suitable for protein hydrolysis in the future by limiting the removal of phosphate PTMs from proteins, and preserving the state of the protein for proteome analysis.

Computational Study of the Hydrolytic Activity of by Zr/Mg MOF-808

Additional DFT calculations were carried out to rationalize the experimentally observed hydrolysis rate

acceleration of both peptide and phosphoester bonds upon incorporation of Mg(II) in the nodes of the MOF.

a) Influence of Mg(II) substitution in Zr-MOF on peptide bond hydrolysis.

The mechanism of peptide hydrolysis catalyzed by Zr-based catalysts has been thoroughly studied by means of experimental and computational methods and is in general well established.[79-82] As schematically shown in Figure 7, it starts with the coordination of the amide oxygen to a Zr(IV) center, which acts as a Lewis acid to polarize the C=O bond, prompting the nucleophilic attack of a water molecule to the C atom. The latter process is commonly assisted by a Brönsted base that can be either the terminal carboxylate group of the dipeptide or a neighboring Zr-hydroxo group. This is followed by a sequence of fast proton transfer events that shift a proton from the group acting as general base to the amide N, ultimately triggering the cleavage of the C—N bond and yielding the products. The whole reaction has been consistently shown to proceed uphill until the transition state (TS) responsible for the C—N bond cleavage is reached, which is the rate-limiting TS of the catalytic cycle.[76] Harvey and coworkers analyzed the mechanism of Gly-Gly hydrolysis catalyzed by MOF-808 relying on DFT calculations.[82] This work identified the coordination of Gly-Gly to two Zr centers in the metal-oxo nodes via the carboxylate function as the most stable binding mode of Gly-Gly to the MOF catalyst. In fact, this species was proposed to act as the resting state of the catalyst, from which the overall free-energy barrier to reach the TS for C—N cleavage determines the reaction rate.

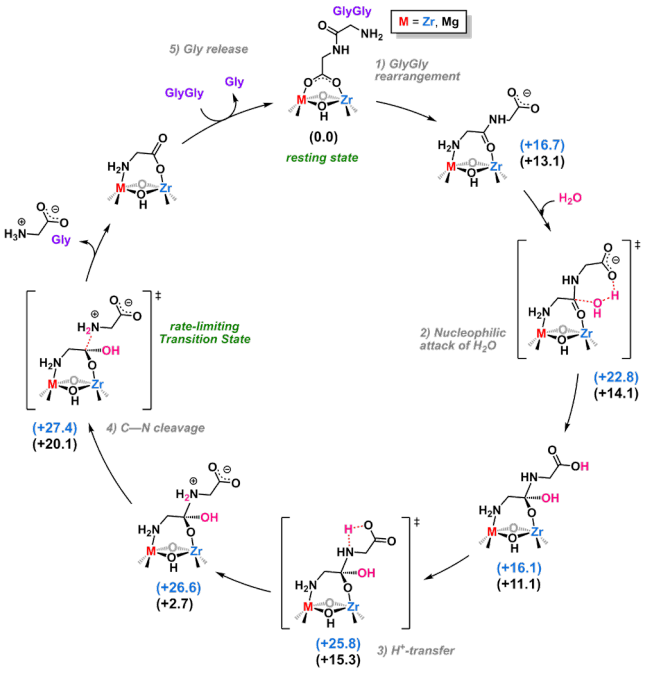

Figure 7: Schematic representation of the catalytic cycle for Gly-Gly hydrolysis promoted by Zr and **Mg1-Zr** MOF-808-based catalysts. Relative Gibbs free energies are given in kcal.mol^{-1} for both **Zr** (blue values) and **Mg1-Zr** (black values) systems. See Figure S9 for a 3D representation of the key transition states and intermediates.

On these grounds, the following calculations using Gly-Gly as a model substrate, focus on comparing the energetic features of the catalytic cycle represented in Figure 7 to elucidate the impact of the metal substitution on the catalytic performance of the MOF towards Gly-Gly hydrolysis. As the hydrolysis of Gly-Gly takes place in water, fully hydrated configurations of the nodes were considered, in which all acetate ligands are replaced by hydroxo and aqua ligands disposed in an alternate fashion. As shown in Figure 7, the rearrangement of Gly-Gly to enable the activation of the peptide bond entails a slightly higher free-energy cost for **Zr** than for **Mg1-Zr** ($\Delta G°$ of +16.7 vs +13.1 kcal.mol^{-1}, respectively). An alternative configuration whereby the amide oxygen binds to the Mg(II) center and the terminal amino group coordinates to the Zr(IV) ion was found to be less stable by 1.4 kcal.mol^{-1}. Despite this small energy difference, the disctinct reactivity of these two binding modes is reflected in the partial charges supported by the amide carbon (+0.59 and +0.57 when coordinated to Zr and Mg, respectively) and in the lenght of the C=O bond (1.27 and 1.26 Å when coordinating to Zr and Mg, repectively), indicating that the amide group is activated to a greater extent when bound to the stronger Zr(IV) Lewis acid site.

The following nucleophilic attack of a water molecule to the C atom of the peptide bond, assisted by the terminal carboxylate group of Gly-Gly as a Brönsted base, involves a barrier of 6.1 kcal.mol^{-1} for **Zr**, whereas the analogous barrier for **Mg1-Zr** is significantly lower (1.0 kcal.mol^{-1}). This suggests that indeed, incorporating a Mg(II) ion within the MOF's node has a beneficial impact on increasing the Lewis acidity of its neighboring Zr(IV) ion, as a result of the decrease of its coordination number discussed above. Accordingly, the following tetrahedral intermediate is also more stable for the **Mg1-Zr** catalyst (by 5.0 kcal.mol^{-1}), as compared to **Zr**. From this intermediate, a proton transfer from the terminal carboxylic acid group to the peptide nitrogen further weakens the C—N bond, promoting its cleavage in a stepwise process. In the case of **Zr**, the proton transfer proceeds uphill, resulting in a transient, shallow zwitterionic intermediate that rapidly evolves toward the rate-determining TS associated with the C—N bond cleavage. Note that although such a zwitterionic intermediate lies 1.3 kcal.mol^{-1} below the proton-transfer TS in terms of electronic energy, thermal and entropic corrections raise its Gibbs free energy 0.6 kcal.mol^{-1} above that of the TS (Figure 7). In contrast, the structural features of the **Mg1-Zr** nodes can more effectively stabilize the analogous zwitterionic intermediate through the formation of hydrogen bonds between the intermediate and structural oxygen atoms of the metal-oxo cluster (compare Figure S9e-f). However, achieving the C—N cleavage TS configuration from this intermediate more substantial structural distortion in **Mg1-Zr** compared to **Zr**.

Beyond these subtle mechanistic differences, and most importantly, the overall free energy calculated from the resting state to the rate-limiting TS (see Figure 7) was found

to be significantly lower for the Mg-containing MOF catalyst, in agreement with the experimentally observed increase in reaction rate.

Specifically, the calculated overall free-energy barriers are 27.4 and 20.1 kcal.mol^{-1} for **Zr** and **Mg1-Zr**, respectively. Grasping a full picture of the reaction mechanism allows us to propose that the observed difference in the reaction rate is due to increased Lewis acidity of the Zr(IV) ion in **Mg1-Zr** that participates in the reaction, compared to those present in **Zr**. This increased acidity facilitates the nucleophilic attack step, thus shifting down in energy the subsequent intermediates and TSs, leading to a lower, overall free-energy barrier. However, if this were to be the only factor leading to enhanced reactivity, undercoordinated Zr(IV)/Zr(IV) sites in **Mg1-Zr** should display reactivity similar to that of Mg(II)/Zr(IV) sites. However, an overall free-energy barrier of 25.6 kcal.mol^{-1} was determined for Zr(IV)/Zr(IV) sites in **Mg1-Zr**, which is indeed lower compared to the free-energy barrier obtained for Zr(IV)/Zr(IV) sites in **Zr** (27.4 kcal.mol^{-1}), but still higher than that obtained for Mg(II)/Zr(IV) sites (20.1 kcal.mol^{-1}). Therefore, this indicates that beyond increasing the Lewis acidity of the neighboring Zr center, Mg also plays a secondary role in destabilizing of the resting state by granting a weaker interaction between the carboxylate function of the substrate and the Mg/Zr site compared to Zr/Zr sites, thus enhancing the activity of the material. This effect can be appreciated in the free-energy cost of the first step of the reaction, whereby the carboxylate-site interaction is lost (Figure 7). This accounts for +16.7, +16.2 and +13.1 kcal.mol^{-1} for Zr/Zr sites in **Zr**, Zr/Zr sites in **Mg1-Zr** and Mg/Zr sites in **Mg1-Zr**, respectively, thus being more than 3 kcal.mol^{-1} lower when Mg is directly involved in the coordination. Further validating the above conclusions, the calculated zero-point energy-corrected electronic energy barriers (EZPE‡), in the absence of thermal and entropic effects, are 19.7 and 11.6 kcal.mol^{-1} for **Zr** and **Mg1-Zr**, respectively, which is in rather good agreement with the experimental activation energies of 18.0 and 13.9 kcal.mol^{-1}. Hence, this supports that the structural model proposed for Mg-containing nodes is sound and that here reported DFT calculations can qualitatively, if not quantitatively, explain the enhanced hydrolytic activity of the Mg-containing material. One should note as well, that the experimentally measured E_a for **Mg1-Zr** may account for a weighted average of reaction paths taking place through both Mg(II)/Zr(IV) and Zr(IV)/Zr(IV) sites and thus, it is expected that the calculated barrier on a Mg(II)/Zr(IV) site underestimates the experimental one. In fact, calculated barrier of 11.6 kcal.mol^{-1} is closer to the experimental Ea of 12.1 kcal.mol^{-1} that was determined for **Mg2-Zr** that contains *ca.* two Mg(II) ions per node, and is expected to show a greater contribution from Mg(II)/Zr(IV) sites.

b) *Influence of Mg(II) substitution in Zr-MOF on phosphoester bond hydrolysis.*

Similar conclusions can be inferred from the analysis of the phosphoester bond hydrolysis in pSer. Based on reported acidity constants of pSer,[83] we considered the binding of its monoanionic, monoprotonated form to the MOF, exploring the possible abstraction of its last proton by hydroxo ligands of the MOF's node as well. Initially, we compared different coordination modes and configurational isomers for the monoanionic pSer binding to the MOF, as depicted in Figure S16. The mono-dentate coordination though a PO group of pSer to a Zr site was found to represent the most stable binding mode for **Zr** and **Mg1-Zr**, with only slight energy differences. Unlike Gly-Gly hydrolysis, the carboxylate binding mode towards the **Zr** and **Mg1-Zr** catalysts is significantly less favored with a relative energy of 32.3 and 13.9 kcal.mol^{-1}, respectively.

Then, we characterized the mechanism of phosphoester hydrolysis by the MOF, based on previous extensive computational studies.[84-86] The catalytic cycle is summarized in Figure 8. Initially, a phosphate oxygen of the monoprotonated pSer substrate coordinates to a Zr(IV) center, transferring a proton to the hydroxo ligand of the vicinal metal center. Subsequently, the phosphoester substrate can rearrange, establishing a hydrogen bond between a phosphate oxygen and the aqua ligand coordinated to the vicinal metal site. This resulting structure represents the resting state for **Mg1-Zr**. Akin to the GlyGly substrate (vide supra), the binding of pSer to the cluster through its phosphoryl group is more likely to involve the Zr(IV) center rather than the Mg(II) one, with an energy difference of 25.0 kcal.mol^{-1}. Conversely, the resting state for **Zr** consists in a monoprotanted pSer coordinated to a Zr(IV) center, in which the neighboring Zr(IV) site bears a hydroxyl ligand. Such a difference most likely arises from the increased Brönsted basicity of Mg(II)-coordinated hydroxyl groups compared to Zr(IV)-bound ones.

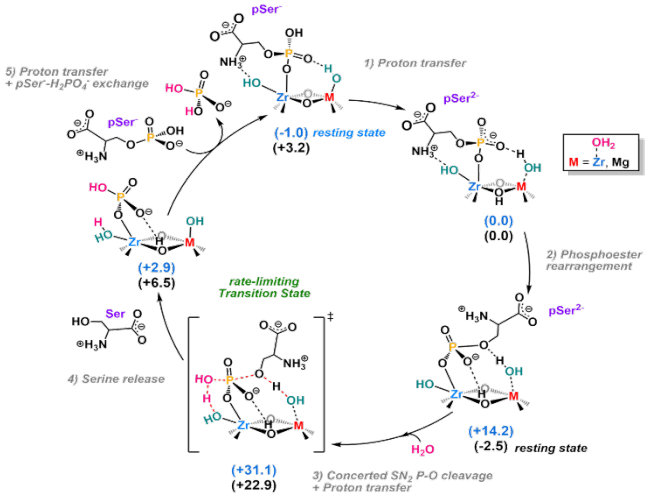

Figure 8: Schematic representation of the catalytic cycle for the phosphoester hydrolysis in pSer catalyzed by**Zr** and **Mg1-Zr**. Relative Gibbs free energies (kcal.mol^{-1}) are given in blue and black, for **Zr** and **Mg1-Zr** catalysts, respectively.

The rate-determining step of the cycle involves the nucleophilic attack of an external water molecule to the P atom of pSer, which occurs concomitantly with the cleavage of a P-O bond through a concerted transition state, following a SN_2

mechanism. This process is assisted by a hydroxo ligand bound to the same Zr center as the substrate, which abstracts a proton from the attacking water molecule; and by a vicinal Zr/Mg-aqua group, which protonates the alkoxide leaving group, releasing Ser. Thus, the overall free energy calculated from the resting state of each system to the rate-limiting TS is significantly lower for the **Mg1-Zr** MOF showing consistency with the experimental kinetic data for the pSer hydrolysis (main text, Table 4). The obtained barriers were 32.1 and 25.4 kcal/mol^{-1} for **Zr** and **Mg1-Zr**, respectively, with the hydrolysis barrier being 6.5 kcal/mol^{-1} lower for the hydrolysis for the Zr-Mg pair sites. The introduction of Mg into the Zr-MOF similarly benefits this reaction as observed for the Gly-Gly hydrolysis, increasing the Lewis acidity of the Zr(IV) center where pSer gets coordinated, lowers the barrier of the rate-determining transition state as phosphorus gets more electrophilic facilitating the nucleophilic attack of a water group. Although the aqua ligand on the Mg(II) center is less acidic, it does not have impact the overall Gibbs free-energy barrier due to the high basicity of the Ser-leaving group. The final stage of the catalytic cycle involves proton transfer from the Zr aqua ligand to the coordinated HPO_4^{2-} group, which is subsequently exchanged for a pSer- substrate to restart the catalytic cycle.

Conclusion

In conclusion, through in-depth structural analysis and computational methods, we have demonstrated that post-synthetic exchange of Mg(II) into Zr_6O_8 based-MOF-808 produces both Zr_5MgO_8 and $Zr_4Mg_2O_7$ clusters within the MOF structure. Detailed XAFS analysis confirmed full incorporation of Mg(II) in place of Zr(IV) in the clusters, which resulted in a reduced oxygen coordination of 7.3 and 6.8 for Zr_5MgO_8 and $Zr_4Mg_2O_7$ respectively, compared to 8 for Zr_6O_8 based MOF-808. This is further supported by computational studies combining DFT calculations with DFT-MD simulations, which suggest that such a metal-exchange process is thermodynamically feasible. Moreover, these calculations provided a structural model of Mg-containing nodes, revealing that embedded Mg(II) ions are found in a distorted octahedral environment, yet without compromising the structural integrity of metal-oxo nodes. Other structural features such as missing linker defects and particle size were similar for all MOFs with and without incorporated Mg(II), but the PSE process reduced the acidity of MOFs, as expected when strongly Lewis acidic Zr(IV) is replaced with Mg(II). However, when the hydrolytic activity was tested towards hydrolysis of peptide and phosphoester bonds in biological molecules, the structural modifications around the active sites promoted by incorporation of Mg(II) significantly benefited the reactivity of the MOFs, despite the much lower Lewis acidity of Mg(II) compared to Zr(IV). The DFT calculations of the reaction mechanisms further confirmed that the replacement of Zr(IV) by Mg(II) ions in the metal-oxo nodes leads to the formation of under-coordinated Zr(IV) sites within the cluster node, which causes the increase of its Lewis acidity and favors the nucleophilic attack of water. Both these factors are essential in peptide and phosphoester bond hydrolysis and therefore their tuning results in the enhancement of catalytic activity. Combining the structural analysis and reactivity findings, it can be further concluded that the reduced oxygen coordination in the Zr5MgO8 and Zr4Mg2O7 clusters caused by the presence of Mg(II) promotes substrate interaction and hydrolysis by creating coordinately unsaturated Zr(IV) metal sites in the cluster. As such, this defines a new avenue for the modulation of the catalytically active sites of MOFs which is distinct from insertion of missing linker defects, and as such, does not reduce the structural stability of the material.

ASSOCIATED CONTENT

Author Information

Corresponding Author

* tatjana.vogt@kuleuven.be

Present Addresses

†Department of Chemistry, University of Antwerp, Universiteitsplein 1, 2610 Wilrijk, Belgium

††Department of Chemistry, Chemistry Research Laboratory, University of Oxford, 12 Mansfield Road, Oxford, OX1 3TA, United Kingdom

Author Contributions

The manuscript was written through contributions of all authors. All authors have given approval to the final version of the manuscript. ‡These authors contributed equally).

Supporting Information

The Supporting Information is available free of charge online. The Supporting Information contains: additional details about experimental procedures, computational details, ICP-OES results for Mg1-Zr and Mg2-Zr post-synthesis, N_2 isotherms, pore size distribution, Rietveld refinement plots and retrieved parameters, FT-IR spectra, TGA curves, experimental pKa values, ^{1}H-NMR spectra, PXRD patterns after hydrolysis reaction.

Acknowledgments

We thank KU Leuven and Research Foundation – Flanders (FWO) for funding. C.S. (68090/11C9320N) and A.M. (1228622N) thank the FWO for fellowships. T.P.N.V. thanks FWO (G025624N and I002720N) for funding. We acknowledge Elettra Sincrotrone Trieste for providing access to its synchrotron radiation facilities (Project no. 20220131, A.M. as PI) and for financial support under the IUS internal project. Moreover, A.M. acknowledges the FWO for an extended research stay grant at the Elettra synchrotron facility (Grant no. V439222N). J. J. C., A. S.-D., and J. P.-J. thank grant PID2021-128128NB-I00, funded by MCIN/AEI/10.13039/501100011033 and by "ERDF A way of making Europe", and the Generalitat de Catalunya (2021SGR00110). A. S.-D. also acknowledges the Spanish Ministry of Universities and the European Union – Next Generation EU for their financial support through a Margarita Salas grant. A. S.-D. also acknowledges financial support from the "la Caixa" Foundation (ID 100010434) under the fellowship code LCF/BQ/PI24/12040012.

REFERENCES

(1) Parshall, G. W.; Putscher, R. E. Organometallic Chemistry and Catalysis in Industry. *Journal of Chemical Education* **1986**, *63* (3), 189 - 191. DOI: 10.1021/ed063p189?

(2) Zheng, H. Q.; Zeng, Y. N.; Chen, J.; Lin, R. G.; Zhuang, W. E.; Cao, R.; Lin, Z. J. Zr-based metal–organic frameworks with intrinsic peroxidase-

like activity for ultradeep oxidative desulfurization: mechanism of H2O2 decomposition. *Inorganic Chemistry* **2019**, *58*, 6983-6992.
(3) García-Serna, J.; Piñero-Hernanz, R.; Durán-Martín, D. Inspirational perspectives and principles on the use of catalysts to create sustainability. *Catalysis Today* **2022**, *387*, 237-243. DOI: 10.1016/j.cattod.2021.11.021.
(4) Bradfield, J. R. G. The Localisation of Enzymes in Cells. *Biological Reviews* **1950**, *25* (1), 113 - 157.
(5) Breaker, R. R. DNA Enzymes. *Nature Biotechnology* **1997**, *15*, 427 - 431.
(6) Tewari, Y. B. Thermodynamics of Industrially-Important, Enzyme-Catalyzed Reactions. *Applied Biochemistry and Biotechnology* **1990**, *23*, 187 - 203.
(7) Lambert, P. W.; Meers, J. L.; Best, D. J. The production of industrial enzymes. *Philosophical Transactions of the Royal Society of London.* **1997**, *300* (1100), 263-282. DOI: 10.1098/rstb.1983.0004.
(8) Vandermarliere, E.; Mueller, M.; Martens, L. Getting intimate with trypsin, the leading protease in proteomics. *Mass Spectrometry Reviews* **2013**, *32* (6), 453-465. DOI: 10.1002/mas.21376.
(9) Niu, X.; Li, X.; Lyu, Z.; Pan, J.; Ding, S.; Ruan, X.; Zhu, W.; Du, D.; Lin, Y. Metal-organic framework based nanozymes: promising materials for biochemical analysis. *Chem Commun (Camb)* **2020**, *56* (77), 11338-11353. DOI: 10.1039/d0cc04890a From NLM Medline.
(10) Huang, Y.; Ren, J.; Qu, X. Nanozymes: Classification, Catalytic Mechanisms, Activity Regulation, and Applications. *Chemical Reviews* **2019**, *119* (6), 4357-4412. DOI: 10.1021/acs.chemrev.8b00672.
(11) Wu, J.; Wang, X.; Wang, Q.; Lou, Z.; Li, S.; Zhu, Y.; Qin, L.; Wei, H. Nanomaterials with enzyme-like characteristics (nanozymes): next-generation artificial enzymes (II). *Chemical Society Reviews* **2019**, *48* (4), 1004-1076. DOI: 10.1039/c8cs00457a.
(12) Huang, X.; Zhang, S.; Tang, Y.; Zhang, X.; Bai, Y.; Pang, H. Advances in metal–organic framework-based nanozymes and their applications. *Coordination Chemistry Reviews* **2021**, *449*. DOI: 10.1016/j.ccr.2021.214216.
(13) Meng, Y.; Li, W.; Pan, X.; Gadd, G. M. Applications of nanozymes in the environment. *Environmental Science: Nano* **2020**, *7* (5), 1305-1318. DOI: 10.1039/c9en01089k.
(14) Gabrielli, L.; Prins, L. J.; Rastrelli, F.; Mancin, F.; Scrimin, P. Hydrolytic Nanozymes. *European Journal of Organic Chemistry* **2020**, *2020* (32), 5044-5055. DOI: 10.1002/ejoc.202000356.
(15) Fang, R.; Liu, J. Cleaving DNA by nanozymes. *Journal of Materials Chemistry B* **2020**, *8* (32), 7135-7142. DOI: 10.1039/d0tb01274b.
(16) Wu, T.; Huang, S.; Yang, H.; Ye, N.; Tong, L.; Chen, G.; Zhou, Q.; Ouyang, G. Bimetal Biomimetic Engineering Utilizing Metal–Organic Frameworks for Superoxide Dismutase Mimic. *ACS Materials Letters* **2022**, *4* (4), 751-757. DOI: 10.1021/acsmaterialslett.2c00075.
(17) Li, S.; Zhou, Z.; Tie, Z.; Wang, B.; Ye, M.; Du, L.; Cui, R.; Liu, W.; Wan, C.; Liu, Q.; Zhao, S.; Wang, Q.; Zhang, Y.; Zhang, S.; Zhang, H.; Du, Y.; Wei, H. Data-informed discovery of hydrolytic nanozymes. *Nature Communications* **2022**, *13* (1). DOI: 10.1038/s41467-022-28344-2.
(18) Farha, O. K.; Eryazici, I.; Jeong, N. C.; Hauser, B. G.; Wilmer, C. E.; Sarjeant, A. A.; Snurr, R. Q.; Nguyen, S. T.; Yazaydin, A. O.; Hupp, J. T. Metal-organic framework materials with ultrahigh surface areas: is the sky the limit? *Journal of the American Chemical Society* **2012**, *134* (36), 15016-15021. DOI: 10.1021/ja3055639.
(19) Czaja, A. U.; Trukhan, N.; Muller, U. Industrial applications of metal-organic frameworks. *Chem Soc Rev* **2009**, *38* (5), 1284-1293. DOI: 10.1039/b804680h From NLM PubMed-not-MEDLINE.
(20) Silva, P.; Vilela, S. M.; Tome, J. P.; Almeida Paz, F. A. Multifunctional metal-organic frameworks: from academia to industrial applications. *Chemical Society Reviews* **2015**, *44* (19), 6774-6803. DOI: 10.1039/c5cs00307e.
(21) Mon, M.; Bruno, R.; Sanz-Navarro, S.; Negro, C.; Ferrando-Soria, J.; Bartella, L.; Di Donna, L.; Prejanò, M.; Marino, T.; Leyva-Pérez, A.; Armentano, D.; Pardo, E. Hydrolase–like catalysis and structural resolution of natural products by a metal–organic framework. *Nature Communications* **2020**, *11* (1), 3080. DOI: 10.1038/s41467-020-16699-3.
(22) Loosen, A.; Simms, C.; Smolders, S.; De Vos, D. E.; Parac-Vogt, T. N. Bimetallic Ce/Zr UiO-66 Metal–Organic Framework Nanostructures as Peptidase and Oxidase Nanozymes. *ACS Applied Nano Materials* **2021**, *4* (6), 5748-5757. DOI: 10.1021/acsanm.1c00546.
(23) Zheng, H. Q.; Zeng, Y. N.; Chen, J.; Lin, R. G.; Zhuang, W. E.; Cao, R.; Lin, Z. J. Zr-Based Metal-Organic Frameworks with Intrinsic Peroxidase-Like Activity for Ultradeep Oxidative Desulfurization: Mechanism of H2O2 Decomposition. *Inorg Chem* **2019**, *58* (10), 6983-6992. DOI: 10.1021/acs.inorgchem.9b00604 From NLM Medline.
(24) Chen, J.; Li, K.; Yang, J.; Gu, J. Bimetallic Ordered Large-Pore MesoMOFs for Simultaneous Enrichment and Dephosphorylation of Phosphopeptides. *ACS Applied Materials & Interfaces* **2021**, *13* (50), 60173-60181. DOI: 10.1021/acsami.1c18201.
(25) Li, P.; Moon, S. Y.; Guelta, M. A.; Lin, L.; Gomez-Gualdron, D. A.; Snurr, R. Q.; Harvey, S. P.; Hupp, J. T.; Farha, O. K. Nanosizing a Metal-Organic Framework Enzyme Carrier for Accelerating Nerve Agent Hydrolysis. *ACS Nano* **2016**, *10* (10), 9174-9182. DOI: 10.1021/acsnano.6b04996.
(26) Islamoglu, T.; Ortuno, M. A.; Proussaloglou, E.; Howarth, A. J.; Vermeulen, N. A.; Atilgan, A.; Asiri, A. M.; Cramer, C. J.; Farha, O. K. Presence versus Proximity: The Role of Pendant Amines in the Catalytic Hydrolysis of a Nerve Agent Simulant. *Angew Chem Int Ed Engl* **2018**, *57* (7), 1949-1953. DOI: 10.1002/anie.201712645 From NLM Medline.
(27) Katz, M. J.; Moon, S. Y.; Mondloch, J. E.; Beyzavi, M. H.; Stephenson, C. J.; Hupp, J. T.; Farha, O. K. Exploiting parameter space in MOFs: a 20-fold enhancement of phosphate-ester hydrolysis with UiO-66-NH2. *Chem Sci* **2015**, *6* (4), 2286-2291. DOI: 10.1039/c4sc03613a From NLM PubMed-not-MEDLINE.
(28) Ardila-Suárez, C.; Perez-Beltran, S.; Ramírez-Caballero, G. E.; Balbuena, P. B. Enhanced acidity of defective MOF-808: effects of the activation process and missing linker defects. *Catalysis Science & Technology* **2018**, *8* (3), 847-857. DOI: 10.1039/c7cy02462b.
(29) Mautschke, H. H.; Drache, F.; Senkovska, I.; Kaskel, S.; Llabrés i Xamena, F. X. Catalytic properties of pristine and defect-engineered Zr-MOF-808 metal organic frameworks. *Catalysis Science & Technology* **2018**, *8* (14), 3610-3616. DOI: 10.1039/c8cy00742j.
(30) Simms, C.; de Azambuja, F.; Parac-Vogt, T. N. Enhancing the Catalytic Activity of MOF-808 Towards Peptide Bond Hydrolysis through Synthetic Modulations. *Chemistry - A European Journal* **2021**, *27* (68), 17230-17239. DOI: 10.1002/chem.202103102.
(31) Dai, S.; Simms, C.; Dovgaliuk, I.; Patriarche, G.; Tissot, A.; Parac-Vogt, T. N.; Serre, C. Monodispersed MOF-808 Nanocrystals Synthesized via a Scalable Room-Temperature Approach for Efficient Heterogeneous Peptide Bond Hydrolysis. *Chemistry of Materials* **2021**, *33* (17), 7057-7066. DOI: 10.1021/acs.chemmater.1c02174.
(32) Ly, H. G. T.; Fu, G.; de Azambuja, F.; De Vos, D.; Parac-Vogt, T. N. Nanozymatic Activity of UiO-66 Metal–Organic Frameworks: Tuning the Nanopore Environment Enhances Hydrolytic Activity toward Peptide Bonds. *ACS Applied Nano Materials* **2020**, *3* (9), 8931-8938. DOI: 10.1021/acsanm.0c01688.
(33) Abednatanzi, S.; Gohari Derakhshandeh, P.; Depauw, H.; Coudert, F. X.; Vrielinck, H.; Van Der Voort, P.; Leus, K. Mixed-metal metal-organic frameworks. *Chemical Society Reviews* **2019**, *48* (9), 2535-2565. DOI: 10.1039/c8cs00337h.
(34) Lammert, M.; Gließmann, C.; Reinsch, H.; Stock, N. Synthesis and Characterization of New Ce(IV)-MOFs Exhibiting Various Framework Topologies. *Crystal Growth & Design* **2017**, *17* (3), 1125-1131. DOI: 10.1021/acs.cgd.6b01512.
(35) Guo, S.-H.; Qi, X.-J.; Zhou, H.-M.; Zhou, J.; Wang, X.-H.; Dong, M.; Zhao, X.; Sun, C.-Y.; Wang, X.-L.; Su, Z.-M. A bimetallic-MOF catalyst for efficient CO2 photoreduction from simulated flue gas to value-added formate. *Journal of Materials Chemistry A* **2020**, *8* (23), 11712-11718. DOI: 10.1039/d0ta00205d.
(36) Rasero-Almansa, A. M.; Iglesias, M.; Sánchez, F. Synthesis of bimetallic Zr(Ti)-naphthalendicarboxylate MOFs and their properties as Lewis acid catalysis. *RSC Advances* **2016**, *6* (108), 106790-106797. DOI: 10.1039/c6ra23143h.
(37) Khan, A.; Shaheen, F.; Roman, M.; Ahmad, R.; Mehboob, K.; Aziz, M. H. Highly redox active mesoporous Ni/Co-organic framework as a potential battery type electrode material for high energy density supercapattery. *Journal of Energy Storage* **2023**, *58*. DOI: 10.1016/j.est.2022.106317.

(38) Nguyen, H. G. T.; Mao, L.; Peters, A. W.; Audu, C. O.; Brown, Z. J.; Farha, O. K.; Hupp, J. T.; Nguyen, S. T. Comparative study of titanium-functionalized UiO-66: support effect on the oxidation of cyclohexene using hydrogen peroxide. *Catalysis Science & Technology* **2015**, *5* (9), 4444-4451. DOI: 10.1039/c5cy00825e.
(39) Castells-Gil, J.; Almora-Barrios, N.; Lerma-Berlanga, B.; Padial, N. M.; Martí-Gastaldo, C. Chemical complexity for targeted function in heterometallic titanium–organic frameworks. *Chemical Science* **2023**, *14* (25), 6826-6840.
(40) Rubio-Gaspar, A.; Navalón, S.; Tatay, S.; Cirujano, F. G.; Fernández-Conde, C.; Padial, N. M.; Martí-Gastaldo, C. Metal Node Control of Brønsted Acidity in Heterobimetallic Titanium–Organic Frameworks. *Journal of the American Chemical Society* **2023**, *145* (7), 3855-3860.
(41) Shakya, D. M.; Ejegbavwo, O. A.; Rajeshkumar, T.; Senanayake, S. D.; Brandt, A. J.; Farzandh, S.; Acharya, N.; Ebrahim, A. M.; Frenkel, A. I.; Rui, N.; Tate, G. L.; Monnier, J. R.; Vogiatzis, K. D.; Shustova, N. B.; Chen, D. A. Selective Catalytic Chemistry at Rhodium(II) Nodes in Bimetallic Metal-Organic Frameworks. *Angew Chem Int Ed Engl* **2019**, *58* (46), 16533-16537. DOI: 10.1002/anie.201908761 From NLM PubMed-not-MEDLINE.
(42) Fu, Y.; Xu, L.; Shen, H.; Yang, H.; Zhang, F.; Zhu, W.; Fan, M. Tunable catalytic properties of multi-metal–organic frameworks for aerobic styrene oxidation. *Chemical Engineering Journal* **2016**, *299*, 135-141. DOI: 10.1016/j.cej.2016.04.102.
(43) Sikma, R. E.; Butler, K. S.; Vogel, D. J.; Harvey, J. A.; Sava Gallis, D. F. Quest for Multifunctionality: Current Progress in the Characterization of Heterometallic Metal–Organic Frameworks. *Journal of the American Chemical Society* **2024**, *146* (9), 5715-5734.
(44) Rego, R. M.; Ajeya, K. V.; Jung, H. Y.; Kabiri, S.; Jafarian, M.; Kurkuri, M. D.; Kigga, M. Nanoarchitectonics of Bimetallic MOF@ Lab-Grade Flexible Filter Papers: An Approach Towards Real-Time Water Decontamination and Circular Economy. *Small* **2023**, *19* (45), 2302692.
(45) Guo, Q.; Li, Y.; Zheng, L.-W.; Wei, X.-Y.; Xu, Y.; Shen, Y.-W.; Zhang, K.-G.; Yuan, C.-G. Facile fabrication of Fe/Zr binary MOFs for arsenic removal in water: High capacity, fast kinetics and good reusability. *Journal of Environmental Sciences* **2023**, *128*, 213-223.
(46) Giménez-Marqués, M.; Santiago-Portillo, A.; Navalón, S.; Álvaro, M.; Briois, V.; Nouar, F.; Garcia, H.; Serre, C. Exploring the catalytic performance of a series of bimetallic MIL-100(Fe, Ni) MOFs. *Journal of Materials Chemistry A* **2019**, *7* (35), 20285-20292. DOI: 10.1039/c9ta01948k.
(47) Loosen, A.; de Azambuja, F.; Smolders, S.; Moons, J.; Simms, C.; De Vos, D.; Parac-Vogt, T. N. Interplay between structural parameters and reactivity of Zr6-based MOFs as artificial proteases. *Chemical Science* **2020**, *11* (26), 6662-6669. DOI: 10.1039/d0sc02136a.
(48) Simms, C.; Savić, N. D.; De Winter, K.; Parac-Vogt, T. N. Understanding the Role of Surfactants in the Interaction and Hydrolysis of Myoglobin by Zr-MOF-808. *European Journal of Inorganic Chemistry* **2022**, *2022* (20). DOI: 10.1002/ejic.202200145.
(49) Wang, S.; Ly, H. G. T.; Wahiduzzaman, M.; Simms, C.; Dovgaliuk, I.; Tissot, A.; Maurin, G.; Parac-Vogt, T. N.; Serre, C. A zirconium metal-organic framework with SOC topological net for catalytic peptide bond hydrolysis. *Nature Communications* **2022**, *13* (1), 1284. DOI: 10.1038/s41467-022-28886-5.
(50) Ly, H. G. T.; Fu, G.; Kondinski, A.; Bueken, B.; De Vos, D.; Parac-Vogt, T. N. Superactivity of MOF-808 toward Peptide Bond Hydrolysis. *Journal of the American Chemical Society* **2018**, *140* (20), 6325-6335. DOI: 10.1021/jacs.8b01902.
(51) Simms, C.; Mullaliu, A.; de de Azambuja, F.; Aquilanti, G.; Parac-Vogt, T. N. Green, Safe, and Reliable Synthesis of Bimetallic MOF-808 Nanozymes With Enhanced Aqueous Stability and Reactivity for Biological Applications. *Small* **2023**, 2307236.
(52) Gil-San-Millan, R.; López-Maya, E.; Platero-Prats, A. E.; Torres-Pérez, V.; Delgado, P.; Augustyniak, A. W.; Kim, M. K.; Lee, H. W.; Ryu, S. G.; Navarro, J. A. R. Magnesium Exchanged Zirconium Metal-Organic Frameworks with Improved Detoxification Properties of Nerve Agents. *Journal of the American Chemical Society* **2019**, *141* (30), 11801-11805. DOI: 10.1021/jacs.9b05571.
(53) Gil-San-Millan, R.; Lopez-Maya, E.; Platero-Prats, A. E.; Torres-Perez, V.; Delgado, P.; Augustyniak, A. W.; Kim, M. K.; Lee, H. W.; Ryu, S. G.; Navarro, J. A. R. Magnesium Exchanged Zirconium Metal-Organic Frameworks with Improved Detoxification Properties of Nerve Agents. *J Am Chem Soc* **2019**, *141* (30), 11801-11805. DOI: 10.1021/jacs.9b05571 From NLM Medline.
(54) Reinsch, H.; Waitschat, S.; Chavan, S. M.; Lillerud, K. P.; Stock, N. A Facile "Green" Route for Scalable Batch Production and Continuous Synthesis of Zirconium MOFs. *European Journal of Inorganic Chemistry* **2016**, *2016* (27), 4490-4498. DOI: 10.1002/ejic.201600295.
(55) Reinsch, H.; Waitschat, S.; Chavan, S. M.; Lillerud, K. P.; Stock, N. A Facile Green Route for Scalable Batch Production and Continuous Synthesis of Zirconium MOFs. *European Journal of Inorganic Chemistry* **2016**, *2016* (27), 4490-4498. DOI: 10.1002/ejic.201600295.
(56) Klet, R. C.; Liu, Y.; Wang, T. C.; Hupp, J. T.; Farha, O. K. Evaluation of Brønsted acidity and proton topology in Zr- and Hf-based metal-organic frameworks using potentiometric acid-base titration. *Journal of Materials Chemistry A* **2016**, *4* (4), 1479-1485. DOI: 10.1039/c5ta07687k.
(57) Toby, B. H.; Von Dreele, R. B. What's new in GSAS-II. *Powder Diffraction* **2014**, *29* (S2), S2-S6. DOI: 10.1017/s0885715614000736.
(58) Furukawa, H.; Gandara, F.; Zhang, Y. B.; Jiang, J.; Queen, W. L.; Hudson, M. R.; Yaghi, O. M. Water adsorption in porous metal-organic frameworks and related materials. *Journal of the American Chemical Society* **2014**, *136* (11), 4369-4381. DOI: 10.1021/ja500330a.
(59) Aquilanti, G.; Giorgetti, M.; Dominko, R.; Stievano, L.; Arcon, I.; Novello, N.; Olivi, L. Operando characterization of batteries using x-ray absorption spectroscopy: advances at the beamline XAFS at synchrotron Elettra. *Journal of Physics D: Applied Physics* **2017**, *50*, 074001. DOI: 10.1088/1361-6463/aa519a.
(60) Filipponi, A.; Cicco, A. D. X-ray-absorption spectroscopy and n-body distribution functions in condensed matter. II. Data analysis and applications. *Physical Review B* **1995**, *52*, 15135.
(61) Filipponi, A.; Di Cicco, A.; Calogero Renzo, N. X-ray-absorption spectroscopy and n-body distribution functions in condensed matter. I. Theory. *Physical Review B* **1995**, *52*, 15122.
(62) Klet, R. C.; Liu, Y.; Wang, T. C.; Hupp, J. T.; Farha, O. K. Evaluation of Brønsted acidity and proton topology in Zr- and Hf-based metal–organic frameworks using potentiometric acid–base titration. *Journal of Materials Chemistry A* **2016**, *4* (4), 1479-1485. DOI: 10.1039/c5ta07687k.
(63) McCullough, J. D.; Trueblood, K. N. The crystal structure of baddeleyite (monoclinic ZrO2). *Acta Crystallographica* **1959**, *12* (7), 507--511. DOI: 10.1107/S0365110X59001530.
(64) Sasaki, S.; Fujino, K.; Takeuci, Y. X-Ray Determination of Electron-Density Distributions in Oxides, MgO, MnO, CoO, and NiO, and Atomic Scattering Factors of their Constituent Atoms. *Proceedings of the Japan Academy* **1979**, *55* (2), 43-48. DOI: 10.2183/pjab.55.43.
(65) Benseghir, Y.; Solé-Daura, A.; Cairnie, D. R.; Robinson, A. L.; Duguet, M.; Mialane, P.; Gairola, P.; Gomez-Mingot, M.; Fontecave, M.; Iovan, D.; Bonnett, B.; Morris, A. J.; Dolbecq, A.; Mellot-Draznieks, C. Unveiling the Mechanism of the Photocatalytic Reduction of CO2 to Formate Promoted by Porphyrinic Zr-Based Metal-Organic Frameworks. *Journal of Materials Chemistry A* **2022**, *10*, 18103-18115. DOI: https://doi.org/10.1039/D2TA04164B.
(66) Simons, M. C.; Vitillo, J. G.; Babucci, M.; Hoffman, A. S.; Boubnov, A.; Beauvais, M. L.; Chen, Z.; Cramer, C. J.; Chapman, K. W.; Bare, S. R.; Gates, B. C.; Lu, C. C.; Gagliardi, L.; Bhan, A. Structure, Dynamics, and Reactivity for Light Alkane Oxidation of Fe(II) Sites Situated in the Nodes of a Metal-Organic Framework. *J Am Chem Soc* **2019**, *141* (45), 18142-18151. DOI: 10.1021/jacs.9b08686 From NLM PubMed-not-MEDLINE.
(67) Chatterjee, A.; Dixit, M. K.; Tembe, B. L. Solvation Structures and Dynamics of the Magnesium Chloride Mg2-Cl-) Ion Pair in Water--Ethanol Mixtures. *Journal of Physical Chemistry A* **2013**, *117*, 8703--8709.
(68) Messner, C. B.; Hofer, T. S.; Randolf, B. R.; Rode, B. M. Structure and dynamics of the Zr4+ ion in water. *Physical Chemistry Chemical Physics* **2011**, *13*, 224--229.
(69) Lowe, B. M.; Maekawa, Y.; Shibuta, Y.; Sakata, T.; Skylaris, C.-K.; Green, N. G. Dynamic behaviour of the silica-water-bio electrical double

layer in the presence of a divalent electrolyte. *Physical Chemistry Chemical Physics* **2017**, *19*, 2687.
(70) Simms, C.; Mullaliu, A.; Swinnen, S.; De Azambuja, F.; Parac-Vogt, T. N. MOF catalysis meets biochemistry: molecular insights from the hydrolytic activity of MOFs towards biomolecules. **2023**, *8* (3), 270--288.
(71) Radzicka, A.; Wolfenden, R. Rates of uncatalyzed peptide bond hydrolysis in neutral solution and the transition state affinities of proteases. *Journal of the American Chemical Society* **1996**, *118* (26), 6105-6109.
(72) Dai, S.; Simms, C.; Dovgaliuk, I.; Patriarche, G. a. T., A.and Parac-Vogt T. N.; Serre, C. Monodispersed MOF-808 Nanocrystals Synthesized via a Scalable Room-Temperature Approach for Efficient Heterogeneous Peptide Bond Hydrolysis. *Chemistry of Materials* **2021**, *33* (17), 7057-7066. DOI: 10.1021/acs.chemmater.1c02174.
(73) Simms, C.; de Azambuja, F.; N. Parac-Vogt, T. Enhancing the Catalytic Activity of MOF-808 Towards Peptide Bond Hydrolysis through Synthetic Modulations. *Chemistry–A European Journal* **2021**, *27*, 17230-17239. DOI: 10.1002/chem.202103102.
(74) Loosen, A.; de Azambuja, F.; Smolders, S.; Moons, J.; Simms, C.; De Vos, D.; Parac-Vogt, T. N. Interplay between structural parameters and reactivity of Zr 6-based MOFs as artificial proteases. *Chemical Science* **2020**, *11* (26), 6662--6669.
(75) Shearer, G. C.; Chavan, S.; Bordiga, S.; Svelle, S.; Olsbye, K. P.; Lillerud, U.; Lillerud, K. P. Defect Engineering: Tuning the Porosity and Composition of the Metal-Organic Framework UiO-66 via Modulated Synthesis. *Chemistry of Materials* **2016**, *28* (11), 3749--3761.
(76) Feng, X.; Himanshu, S.; Krishnaraj, C.; Leus, K.; Wang, G.; Chen, H.; Jia, C.; Van Der Voort, P. Generating Catalytic Sites in UiO-66 through Defect Engineering. *ACS Applied Materials & Interfaces* **2021**, *13* (51), 60715--60735.
(77) Hardian, R.; Dissegna, S.; Ullrich, A.; Llewellyn, P. L.; Coulet, M. V.; Fischer, R. A. Tuning the Properties of MOF-808 via Defect Engineering and Metal Nanoparticle Encapsulation. *Chemistry–A European Journal* **2021**, *27* (22), 6804--6814.
(78) Loosen, A.; Simms, C.; Smolders, S.; De Vos, D. E.; Parac-Vogt, T. N. Bimetallic Ce/Zr UiO-66 Metal-Organic Framework Nanostructures as Peptidase and Oxidase Nanozymes. *ACS Applied Nano Materials* **2021**, *4* (6), 5748-5757. DOI: 10.1021/acsanm.1c00546.
(79) Mihaylov, T. T.; Ly, H. G. T.; Pierloot, K.; Parac-Vogt, T. N. Molecular Insight from DFT Computations and Kinetic Measurements into the Steric Factors Influencing Peptide Bond Hydrolysis Catalyzed by a Dimeric Zr(IV)-Substituted Keggin Type Polyoxometalate. *Inorganic Chemistry* **2016**, *55*, 9316--9328.
(80) Jayasinghe-Arachchige, V. M.; Hu, Q.; Sharma, G.; Paul, T. J.; Lundberg, M.; Quinonero, D.; Parac-Vogt, T. N.; Prabhakar, R. Hydrolysis of chemically distinct sites of human serum albumin by polyoxometalate: A hybrid QM/MM (ONIOM) study. *Journal of computational chemistry* **2019**, *40*, 51--61.
(81) Solé-Daura, A.; Rodríguez-Fortea, A.; Poblet, J. M.; Robinson, D.; Hirst, J. D.; Carbó, J. J. Origin of Selectivity in Protein Hydrolysis by Zr(IV)-Containing Metal Oxides as Artificial Proteases. *Acs Catalysis* **2020**, *10*, 13455--13467.
(82) Conic, D.; Pierloot, K.; Parac-Vogt, T. N.; Harvey, J. N. Mechanism of the highly effective peptide bond hydrolysis by MOF-808 catalyst under biologically relevant conditions. *Physical Chemistry Chemical Physics* **2020**, *22*, 25136--25145.
(83) Zachariou, M.; Traverso, I.; Spiccia, L.; Hearn, M. T. W. Potentiometric investigations into the acid- base and metal ion binding properties of immobilized metal ion affinity chromatographic (IMAC) adsorbents. *The Journal of Physical Chemistry A* **1996**, *100* (30), 12680--12690.
(84) Martins, F. F.; Sánchez-González, Á.; Lanuza, J.; Miras, H. N.; Lopez, X.; Bandeira, N. A.; Gil, A. Probing the catalytically active species in POM-catalysed DNA-model hydrolysis. *Chemistry–A European Journal* **2021**, *27*, 8977--8984.
(85) Lanuza, J.; Sánchez-González, Á.; Bandeira, N. A. G.; Lopez, X.; Gil, A. Mechanistic Insights into Promoted Hydrolysis of Phosphoester Bonds by MoO2Cl2(DMF)2. *Inorganic Chemistry* **2021**, *60*, 11177--11191.
(86) Chen, H.; Liao, P.; Mendonca, M. L.; Snurr, R. Q. Insights into catalytic hydrolysis of organophosphate warfare agents by metal–organic framework NU-1000. *The Journal of Physical Chemistry C* **2018**, *122*, 12362--12368.

Table of Contents

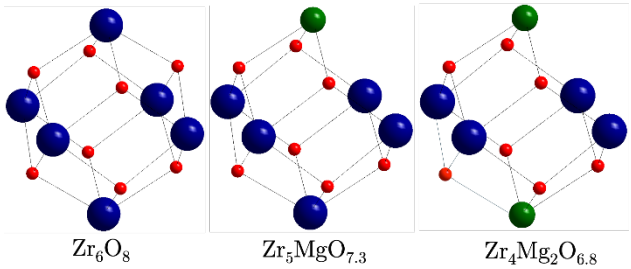

Generation of vacant sites on the inorganic cluster of MOF-808 through exchange of Zr(IV) with Mg(II) results in enhanced catalysis due to lower oxygen occupancy in the cluster originating from the lower coordination number of Mg(II) compared to Zr(IV)